International Journal of Hydrogen Energy 73 (2024) 524–535

Contents lists available at ScienceDirect

International Journal of Hydrogen Energy

journal homepage: www.elsevier.com/locate/he

Effects of secondary air on the emission characteristics of ammonia–hydrogen co-firing flames with LES-FGM method

Liqing Lu [a], Meng Zhang [a,*], Weijie Zhang [a], Lei Chen [b], Pengfei Song [a,b], Zhilong Wei [c], Jinhua Wang [a], Zuohua Huang [a]

[a] State Key Laboratory of Multiphase Flow in Power Engineering, Xi'an Jiaotong University, Xi'an 710049, China
[b] Hainan CO2 Technology Application Center, SINOPEC Gugangzhou Engineering Co. Ltd., China
[c] Mechanical and Electrical Engineering College, Hainan University, China

ARTICLE INFO

Keywords:
Ammonia
Hydrogen
Two-stage combustion
Swirling flames
LES-FGM

ABSTRACT

Ammonia, being a carbon-free fuel, is garnering increasing attention in the combustion community. However, its application is still impeded by its limited stability range and significantly NOx emissions. This study delves into the impact of primary and overall equivalence ratios (ϕ_{pri} and ϕ_{ovr}) on emissions production in ammonia–hydrogen co-firing flames, utilizing a two-stage swirling model gas turbine combustor. The emissions concentration is measured using Fourier Transform Infrared Spectroscopy (FTIR). The physical and chemical processes influencing emissions production are comprehensively analyzed through a combination of Large Eddy Simulation (LES) and Flamelet-Generated Manifold (FGM) method. The reliability of the simulation is validated by the experimental data, showing a good capability in predicting the combustion. Results indicate that the two-stage combustion strategy exhibits significantly controlling effects on NOx and unburned NH_3 emission. The NO emission exhibits a non-monotonic variation with ϕ_{pri}, reaching its lowest value at $\phi_{pri} \approx 1.2$. Further analysis shows that ϕ_{pri} plays a crucial role in determining the temperature and OH concentration in the primary combustion zone, thereby influencing NOx production in this area. When the primary zone is operated at lean condition, the reduction on NO in secondary zone is primarily attributed to dilution effect by the secondary air. In contrast, when $\phi_{pri} > 1$, the concentrations of the main emissions in secondary zone are dominated by chemical effects. In this scenario, unburned NH_3 and H_2 from the primary zone are consumed, resulting in a substantial production of NO in the secondary combustion zone. Additionally, with an increase in ϕ_{pri}, the secondary NO production also increases. The ϕ_{ovr} exhibits two considerable effects. On one hand, an increase in ϕ_{ovr} results in a higher local equivalence ratio in the secondary zone, thereby promoting local NOx production. Simultaneously, the elevated flame temperature enhances the consumption of N_2O. On the other hand, the rise in ϕ_{ovr} results in a reduction in vortex scale and residence time in the secondary combustion zone, leading to a decrease in local NO production.

1. Introduction

The utilization of carbon-free fuels such as hydrogen and ammonia has received much attention in recent years. However, ammonia shows greater advantages compared with hydrogen, since it can be readily liquefied at atmospheric pressure when temperature goes below −33 °C, or at room temperature when pressure is above 8.5 atm. In addition, ammonia benefits from well-established production and transportation infrastructures owing to its extensive industrial usage. Transporting ammonia is significantly safer due to its more moderate storage requirements compared to hydrogen. Hence, ammonia emerges as a promising carbon-free fuel and a suitable hydrogen carrier due to its high hydrogen content [1,2]. However, utilizing ammonia as a fuel presents two challenges, one of them stems from its low burning velocity. Under stoichiometric condition, the laminar flame speed of NH_3-air is merely one-fifth that of methane at 101 kPa and 298 K. This results in poor ammonia combustion stability and diminished combustion efficiency in the combustion chamber. The second challenge arises from ammonia combustion, which yields remarkably elevated NOx emissions in fuel-lean conditions due to the inclusion of nitrogen atoms within the ammonia molecule [3–6].

The issue of flame stabilization of ammonia combustion can be mitigated by introducing reactive fuels, such as hydrogen, into the mixture [7–14]. Zhang et al. [8] investigated the effect of hydrogen

* Corresponding author.
E-mail address: mengz8851@xjtu.edu.cn (M. Zhang).

https://doi.org/10.1016/j.ijhydene.2024.06.009
Received 31 January 2024; Received in revised form 9 May 2024; Accepted 1 June 2024
Available online 11 June 2024

and methane addition on NOx production in NH_3-air flames in a model gas turbine combustor. They showed that adding a small amount of hydrogen to ammonia can significantly broaden the combustion limits of ammonia, and concluded that 10% hydrogen blending is the optimal choice, as it enhances the stability of the ammonia combustion without exacerbating NOx emissions. The concept of ammonia–hydrogen co-firing is motivated not only by hydrogen's capacity to enhance ammonia combustion but also by the fact that it can be produced by partial cracking ammonia which provides a pure carbon-free solution for combustion devices, such as gas turbines. Therefore, investigating ammonia–hydrogen co-firing flames holds paramount importance for the potential utilization of pure ammonia in gas turbines.

In ammonia–hydrogen co-firing flames, the issue of fuel NOx remains prominent, largely attributed to the presence of nitrogen atoms. Zhang et al. [8] reported NO concentrations in excess of 1000 ppm at the combustion chamber outlet for NH_3-H_2-air flames with equivalence ratio (ϕ) ranging from 0.8 to 1.0 at 10% H_2 ratio, which is in agreement with measurements made by Mashruk et al. [15] in an industrial scale tangential swirl burner. However, the experimental results of Khateeb et al. [11] in a generic swirl combustor showed NO emission exceeds 1500 ppm under nearly the same conditions as Zhang et al. [8] and exhibits the peak close to 3000 ppm at $\phi = 0.9$. Fortunately, the results of Okafor et al. [5] showed that the two-stage rich-lean combustion strategy is effective in controlling the fuel NOx. They firstly measured the emissions in NH_3-CH_4-air flames in a single-stage micro gas turbine combustor and found that NOx exceeded 5000 ppm at ϕ ranging from 0.8 to 1.1. Subsequently, they implemented the two-stage rich-lean combustion strategy and achieved NOx emissions below 100 ppm under specific conditions characterized by an overall equivalence ratio ϕ_{ovr} of 0.38, a primary equivalence ratio ϕ_{pri} of 1.30, with the ammonia fraction of 0.3 by calorific value. Somarathne et al. [16,17] also arrived at a similar conclusion through LES calculations under high pressure, revealing that the equivalence ratio in the primary combustion zone plays a decisive role in the ultimate NO emissions in two-stage combustion. Li et al. [2] conducted a combustion reaction network (CRN) analysis to examine the emission characteristics of an ammonia/methane co-firing model combustion chamber using Tian mechanism [18]. The simulation was conducted under operational parameters relevant to H/J-class heavy duty gas turbine conditions. They also emphasized the controlling effects of staged combustion scenario. In the staged combustion case, where ammonia constituted 40% of the volume and the equivalence ratio for the primary fuel-rich stage was set at 1.5, the NOx emission can be significantly decreased to as low as 86 ppm. This is a remarkable reduction, as it was only one-thirteenth of the concentration observed in the single-stage combustion case, which was 1119 ppm. Similar kinetic simulations can also be found in the studies by Li et al. [19,20]. Mashruk et al. [21] modeled a CRN for an industrial-scale two-stage rich-lean combustion system using five commonly used mechanisms for sensitivity analysis of OH, NH_3, and NO. They found that the rich-lean strategy can reduce NOx to approximately 100 ppm while allowing full consumption of unburned fuel in the primary zone. Guteša et al. [22] conducted CRN simulations, theoretical analysis, and experimental research on 70%NH_3-30%H_2 (vol%) rich flames under humidified conditions, demonstrating that this novel approach can provide gas turbine power generation efficiency similar to Dry Low Nitrogen Oxides and humidified methane-based technologies. It ensures flame stability and low NOx emissions. However, the primary concern arises from the low combustion efficiency caused by high NH_3 and H_2 escape during rich combustion. Subsequently, in their study [23], they introduced the Rich Quench Lean (RQL) strategy, constructing a two-stage combustion CRN including internal and external recirculation zones. The introduction of secondary air achieves the consumption of most active species, resulting in NOx emissions of only about 80 ppm and a power generation efficiency of around 59%. This highlights the high promise of ammonia-based blends for gas turbine applications. However, the majority of existing studies continue to concentrate on the cofiring of methane–ammonia fuels, inevitably contributing to carbon emissions. In the face of the escalating global carbon emissions crisis, the adoption of pure carbon-free fuels becomes imperative to meet future development needs. Hydrogen, being inherently carbon-free, can be directly obtained through ammonia cracking. Moreover, as previously mentioned, the incorporation of 10% hydrogen significantly enhances the stability of pure ammonia flames. Therefore, this study embraces the two-stage combustion strategy to manage emissions in ammonia–hydrogen co-firing flames (10% H_2).

This paper investigates the impacts of primary and overall equivalence ratios on the production and emission of NOx and unburned NH_3 through ammonia–hydrogen two-stage combustion. Emissions concentrations are measured using FTIR. In-depth analysis of emissions production mechanisms is performed utilizing the LES-FGM method. The structure of the paper is outlined as follows. Section 2 introduces the experimental and numerical simulation methodologies employed in this study. In Section 3, a comparison between the simulation results and experimental measurements is conducted firstly to validate the accuracy of the numerical model. Subsequently, the analysis primarily focuses on the influence mechanisms of ϕ_{pri} and ϕ_{ovr} on emissions production from the perspective of LES, elucidating the underlying mechanisms of the observed changes in emissions. Finally, Section 4 provides a comprehensive summary of the entire study.

2. Experimental setup and numerical methods

2.1. Two-stage combustion

The configuration of the swirl combustor utilized in this study is shown in Fig. 1(a) and (b). After thorough mixing in the premixed burner, the fuel and air enter the combustion chamber through an axial swirler. Detailed information about the structure of this burner can be found in our previous works [24,25]. The secondary air is introduced through tangential holes located at the combustor walls to facilitate staged combustion. The combustor side walls were constructed with square quartz glasses, with 70 mm in width, 180 mm in height, and 5 mm in thickness. This design enables easy visualization of the flame structure and facilitates the application of laser diagnostics. The secondary air holes are located on the same side of each wall to avoid the collision of the four air streams and the disturbance of the internal recirculation zone (IRZ) [16]. The hole has a diameter of 13 mm, with its center located 90 mm from the bottom surface of the combustor and 17.5 mm away from the central axis of the glass panel. The swirler employed in this study features an inner diameter of 18 mm, an outer diameter of 35 mm, and a total of 12 blades with a 45° angle. Its swirl number is calculated to be 0.73 based on the formula presented in Eq. (1).

$$S = \frac{2}{3} \cdot \frac{1-(D_i/D_o)^3}{1-(D_i/D_o)^2} \tan\alpha \tag{1}$$

where D_i is the inner diameter of the swirler, D_o is the outer diameter of the swirler, and α is the angle of the blades.

In the experimental process, achieving single-stage combustion involves directing all fuel and air through the swirler into the combustion chamber. For two-stage combustion operation, in addition to the mentioned airflow, there is an additional stream of air entering through secondary air holes. Whether it is single-stage or two-stage combustion, we use ϕ_{pri} to represent the equivalence ratio calculated for the amount of air and fuel entering through the swirler, and ϕ_{ovr} to represent the equivalence ratio calculated for all air and fuel supplied to the combustion chamber. Clearly, for single-stage combustion, $\phi_{pri} = \phi_{ovr}$.

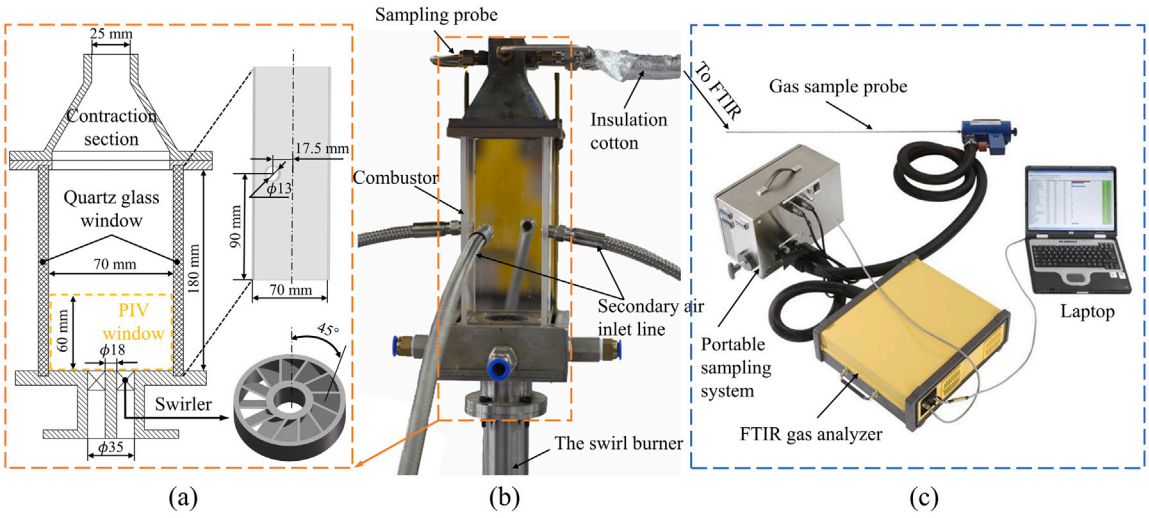

Fig. 1. Schematic diagram of the experimental setup. (a) Structure of the swirl combustion chamber; (b) Photograph of the staged combustion chamber; (c) FTIR system.

2.2. FTIR measurements

This study employs a Gasmet DX4000 Fourier Transform Infrared (FTIR) gas analyzer to measure the concentrations of NOx and unburned NH_3. The schematic diagram of the measurement setup is shown in Fig. 1 (c). FTIR operates on the principle of Fourier transform of infrared light after interference and comprises the Gasmet Portable Sampling System (PSS) and the gas analyzer. Before experimental measurements, the sampling pump, heated filter, and valves are preheated to 453 K (180 °C) to ensure that sampling remains in the gaseous state. Nitrogen is then used for automatic background calibration through PSS. During measurements, the stainless steel sampling probe is connected to the contracted section at the combustor exit. To prevent condensation of water vapor in the pipeline, the sampling probe is continuously heated using a ribbon heater [26]. In order to obtain accurate measurement results, it should be ensured that the measurement time is long enough to stabilize the measured values. Subsequently, the average of these stabilized values is considered the measured emission concentration. In this particular experiment, each individual measurement extended beyond 2 min to achieve this stability. The uncertainties of the FTIR measurements are not larger than 50 ppmv for NO and NH_3, and not larger than 10 ppmv for N_2O and NO_2.

2.3. PIV measurements

To validate the LES results, we conducted Partial Imaging Velocimetry (PIV) experiments on a 10%H_2 single-stage flame with ϕ = 0.8. The PIV system employed a dual-cavity Nd:YAG laser (Litron), a guiding beam arm, a particle generator, and a double shutter CCD camera (Imager LX 2M). The Nd:YAG laser emitted dual-pulsed laser beams with a wavelength of 532 nm, pulse energy of 2 × 300 mJ, and repetition rate of 10 Hz. The formation height of the laser sheet was approximately 60 mm with a thickness of about 1 mm. Titanium dioxide (TiO_2) particles with a diameter of approximately 0.5 μm and a Stokes number of approximately 2×10^{-3} were introduced into the flow field as tracers. The CCD camera with a macro lens (100 mm, F/2.8) captured the Mie scattering signals through a narrow-bandpass filter (LaVision, 532 ± 5 nm, bandwidth of 10 nm). The original image size was 1600 × 1200 pixels with a resolution of 0.058 mm/pixel.

2.4. Numerical simulation methods

This study involves a secondary air supply to achieve the two-stage combustion. As a result, the mixture fraction Z and the progress variable PV (represented as γ later) are selected as control variables in the FGM method. In this context, γ characterizes the transient process of the mixture from unburned to burned and is defined by a linear combination of mass fractions [27–29]:

$$\gamma = \sum_{i=1}^{N_s} \alpha_i Y_i \tag{2}$$

where N_S is the number of species, α_i is the weighting factor and Y_i is the mass fraction of species i. The combination of mass fractions can be chosen arbitrarily as long as it is ensured that γ is monotonic throughout the combustion process. In this work, the mass fraction of water, resulting from the complete combustion of the fuel, is selected for characterization. Specifically, α_{H2O} is assigned a value of $-100M_{H2O}^{-1}$, where M_{H2O} represents the molecular mass of water.

For carbon-free fuels such as NH_3 and H_2, the mixture fraction Z can be expressed in terms of the mass fractions of the elements H, N and O, as shown in Eq. (3) [17]:

$$Z = \frac{0.25M_H^{-1}(Z_H - Z_{H,2}) + 0.75M_N^{-1}(Z_N - Z_{N,2}) - M_O^{-1}(Z_O - Z_{O,2})}{0.25M_H^{-1}(Z_{H,1} - Z_{H,2}) + 0.75M_N^{-1}(Z_{N,1} - Z_{N,2}) - M_O^{-1}(Z_{O,1} - Z_{O,2})} \tag{3}$$

where Z_H, Z_N and Z_O represent the mass fractions of the elements H, N and O, respectively. M_H, M_N and M_O are the atomic masses of the corresponding elements. The subscripts 1 and 2 in Eq. (3) represent the fuel and oxidizer, respectively.

Upon establishing the aforementioned control variables, the one-dimensional flame calculation tool Chem1D [30] coupled with the detailed chemical reaction mechanism proposed by Nakamura et al. [31], which contains 38 species and 232 steps of reactions, is used to calculate the laminar flamelets with different Z and γ. This mechanism has been tested and shown to effectively predict laminar burning velocity [32], ignition delay time [32,33], and concentrations of major emissions [34] in ammonia–hydrogen co-firing flames. The equivalence ratio ϕ is varied from 0.5 to 1.6 to calculate the adiabatic flamelets at T_u = 300 K for different values of mixture fraction. Additionally, the mixture fraction needs to be extrapolated to zero to simulate the secondary air. Subsequently, these flamelets are synthesized to construct a manifold, thereby obtaining thermochemical parameters associated with these two control variables. The relationship between the temperature with respect to the control variables Z and γ is shown in Fig. 2.

The database is coupled in the FGM solver based on OpenFOAM-2.3.x. The resolved equations governing mass, momentum, and control

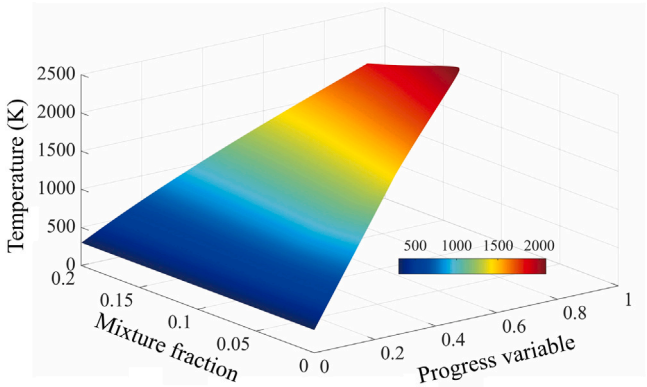

Fig. 2. Temperature along the 2D Z-PV manifold.

variables C_k (= 1, 2, … N_{cv}) are given in Eqs. (4)–(6) [28,29]:

$$\frac{\partial \widehat{\rho}}{\partial t} + \nabla \cdot (\widehat{\rho}\widetilde{\boldsymbol{u}}) = 0 \tag{4}$$

$$\frac{\partial}{\partial t}(\widehat{\rho}\widetilde{\boldsymbol{u}}) + \nabla \cdot (\rho\widetilde{\boldsymbol{u}}\widetilde{\boldsymbol{u}}) = -\nabla p + \nabla \cdot \boldsymbol{\sigma} + \rho \boldsymbol{g} \tag{5}$$

$$\frac{\partial}{\partial t}(\widehat{\rho}\widetilde{C}_k) + \nabla \cdot (\rho\widetilde{\boldsymbol{u}}\widetilde{C}_k) = \nabla \cdot \left[\left(\widehat{\left(\frac{\lambda}{c_p}\right)} + \frac{\mu_t}{Sc_t} \right) \nabla \widetilde{C}_k \right] + \hat{\dot{\omega}}_{Ck} \tag{6}$$

where ρ is the density, $\boldsymbol{u}$ is the velocity vector, p is the pressure, $\boldsymbol{\sigma}$ is the stress tensor, $\boldsymbol{g}$ is the gravitational acceleration, λ is the thermal conductivity, c_p is the constant-pressure specific heat, μ_t is the turbulent eddy viscosity, S_{C_t} is the turbulent Schmidt number which is assumed to be S_{C_t} = 0.7 in this study. $\dot{\omega}_{Ck}$ is the reaction source term, which is non-zero only for the progress variable equation, and is zero for all other control variable equations.

Furthermore, due to the relatively slower rate of NO production compared to other species, predicting the concentration of NO by solely retrieving the database can be challenging. Hence, to improve the accuracy of NO emission prediction in this study, an additional NO transport equation is introduced [26,35], as indicated in Eq. (7).

$$\frac{\partial}{\partial t}(\widehat{\rho}\widetilde{Y}_{NO}) + \nabla \cdot (\widehat{\rho}\widetilde{u}\widetilde{Y}_{NO}) = \nabla \cdot \left[\left(\widehat{\left(\frac{\lambda}{c_p}\right)} + \frac{\mu_t}{Sc_t} \right) \nabla \widetilde{Y}_{NO} \right] + \left(\widehat{\frac{\omega^c_{NO}}{Y^{tab}_{NO}}} \right) \widetilde{Y}_{NO} + \hat{\dot{\omega}}^p_{NO} \tag{7}$$

where Y_{NO} is the NO mass fraction obtained by solving the transport equation, Y^{tab}_{NO} is the NO mass fraction obtained from the database, $\dot{\omega}^c_{NO}$ is the NO consumption source term, and $\dot{\omega}^p_{NO}$ is the NO production source term.

The computational domain for this study is shown in Fig. 3. The simulation employs a structure mirroring the experimental setup with certain simplifications to the combustor and secondary air supply system to lower computational expenses. The premixed gas is directly supplied to the swirler and then enters the combustor, eliminating the need to calculate the gas mixing process inside the burner. Additionally, square holes are used in the combustor wall instead of circular holes to improve the quality of the structured grid. Moreover, an extra large-space was extended from the exit of the combustor to prevent the non-physical backflow (not shown in Fig. 3). The entire computational domain is meshed with the structured grid methodology. Grid refinement is applied to the flame region and small-scale structural areas such as swirler and gas inlets, ensuring that the minimum grid spacing is below 0.3 mm. The total number of grids is approximately 4.2 million, with a maximum skewness not exceeding 1.8 and a minimum grid quality above 0.35.

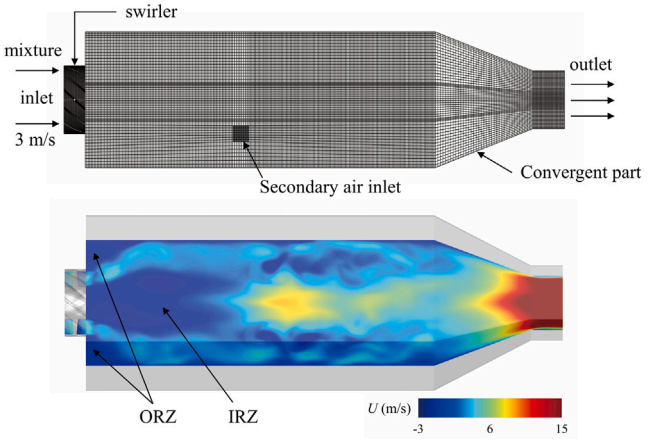

Fig. 3. The computational domain used in this study.

Table 1
The computational conditions for LES.

Pattern	U_{in} (m/s)	Z_{H2} (%)	ϕ_{pri}	ϕ_{ovr}
Single stage	3	10	0.8	–
Two stages	3	10	0.8, 1.0, 1.2, 1.4	0.4
	3	10	1.2	0.35, 0.45, 0.5

2.5. Simulation settings

During the calculation process, it is assumed that both the swirler and the combustion chamber walls are non-slip adiabatic boundaries. The inlet boundary is specified as a velocity inlet, with turbulence generated at the swirl inlet using the LEMOS turbulent generator to mimic experimental conditions. The inlet turbulence intensity, integral length scale, and Reynolds stress tensor field obtained from hot-wire anemometer measurements at the swirler inlet are used as inputs. The outlet pressure is set as a waveTransmissive boundary to avoid reflections. All cases maintain a constant hydrogen blending ratio (volume fraction) Z_{H2} = 0.1. The swirl inlet maintains an average flow velocity of 3 m/s to ensure uniform fluid residence time. Meanwhile, this flow velocity ensures thorough reaction of NH_3, thereby boosting combustion efficiency. The velocity of the secondary air can be computed by considering the predetermined ϕ_{ovr} in conjunction with ϕ_{pri}.

The time step of all cases is set to 2×10^{-6} s to ensure that the maximum Courant number remains below 0.3. Each case is initially simulated in the cold state for a duration of 100 ms before transitioning to the hot state upon ignition, continuing until a steady state is achieved. The cases calculated in this study are shown in Table 1. A single-stage 10%H_2 flame is first calculated to compare with the PIV results to verify the reliability of the simulation method. The effect of ϕ_{pri} (ϕ_{ovr}) on the emissions from ammonia–hydrogen co-firing flames is then explored using staged combustion with fixed ϕ_{ovr} (ϕ_{pri}).

3. Results and discussions

3.1. Simulation validation

In order to validate the reliability of the LES-FGM method, the simulation results of the flow field of single-stage combustion are firstly compared with the experimental results. Fig. 4 presents a comparison of the mean velocity and root-mean-square (RMS) of the flow field at different heights in the central cross-section of the combustor. The black solid lines represent the computational results, while the red dots represent the PIV measurements. Based on Fig. 4(a) and (b), it is evident that the numerical and experimental mean velocity profiles exhibit a favorable consistency. The two peaks of the mean axial

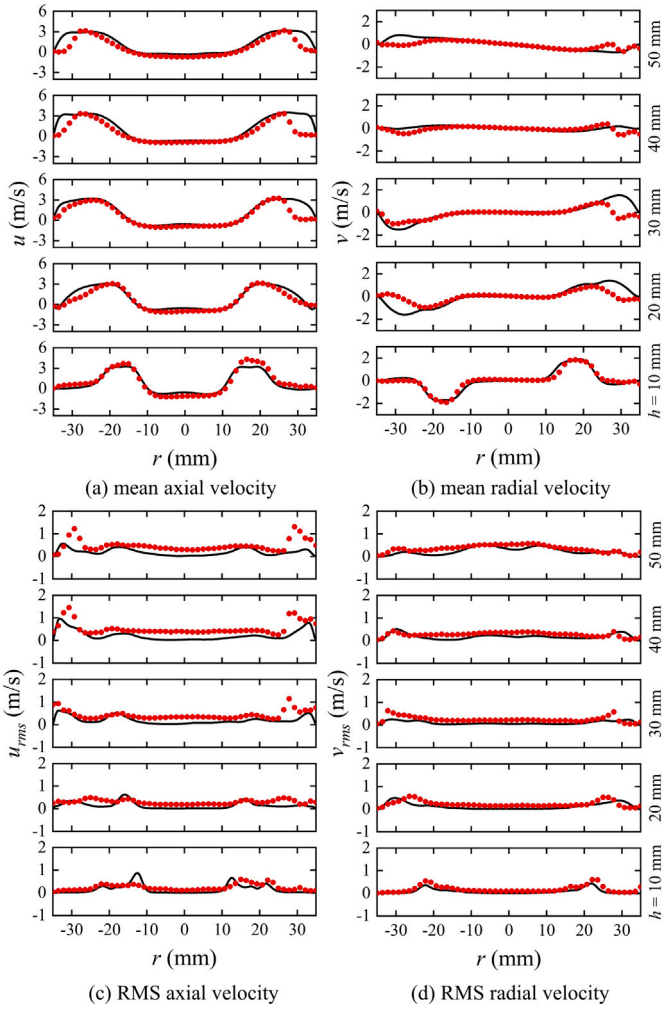

Fig. 4. Comparison of the flow fields between LES results and PIV measurements (black solid lines: LES results, red dots: PIV measurements). The flame was operated under single-stage combustion conditions with ϕ_{pri} = 0.8. (For interpretation of the references to color in this figure legend, the reader is referred to the web version of this article.)

velocity profile are well predicted by the simulation. In addition, the positive and negative peaks of mean radial velocity profiles are also well captured. LES also exhibits a comparable turbulence intensity level in the combustion chamber as the experiments as shown in Fig. 4(c) and (d). In the near-wall region, the discrepancy between the simulation and experiment is primarily attributed to the uncertainties of heat loss applied in the simulation, which is hardly estimated in the experiment. In summary, the present LES method can replicate the experimental velocity fields for all cases.

3.2. Flame structure and emission characteristics

Fig. 5 displays direct digital images of NH_3 flames, 10%H_2 flames, and 20%H_2 flames at various ϕ_{pri} within the stable combustion range at ϕ_{ovr}= 0.4. It is evident that the addition of 10% H_2 significantly enhances the stability limits of NH_3 flame. For 10%H_2 flames, although the flame exhibits some instability at ϕ_{pri} = 1.4, the NOx emission and unburned NH_3 are relatively low, as will be discussed in details below. From a macroscopic perspective, ammonia flames typically exhibit orange chemiluminescence owing to spectral radiation from the $NH_2\alpha$ band and superheated water vapor [36]. As the proportion of hydrogen increases, the flame color tends towards whitish and approaches transparency. This change is likely attributed to the

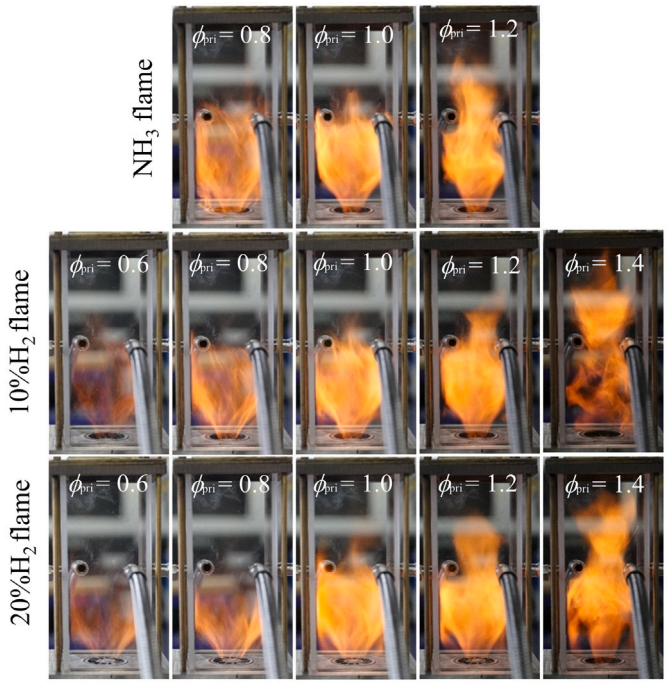

Fig. 5. Digital photographs of flames under various primary equivalence ratios ϕ_{pri} for NH_3 flames, 10%H_2 flames, and 20%H_2 flames. The overall equivalence ratio is maintained at ϕ_{ovr} = 0.4.

increased participation of OH and H radicals in reactions. Additionally, as depicted in Fig. 5, it can be observed that under each hydrogen ratio, the flames are sustained upstream in the combustion chamber at fuel-lean conditions of the primary equivalence ratio (primary-lean conditions). As ϕ_{pri} exceeds 1.0 (primary-rich conditions), the flames begin to propagate downstream and are located higher than secondary air holes. This behavior suggests potential secondary combustion of ammonia following secondary air injection, a phenomenon that will be further detailed in Section 3.3.

Fig. 6 illustrates the variation in NOx and unburned NH_3 emissions with ϕ_{pri} derived from both experiments and simulations. The black, blue, and red lines denote the experimental results for single-stage combustion, two-stage combustion, and the simulated results for two-stage combustion, respectively. In the context of single-stage combustion, NO concentration peaks around ϕ_{pri} = 0.85 and gradually diminishes as ϕ_{pri} goes to either lean or rich side. Furthermore, beyond ϕ_{pri} > 1.1, the inhibition of fuel NO generation causes the NO concentration to drop below 100 ppm. N_2O is elevated under fuel-lean conditions, experiencing a notable reduction by increasing ϕ_{pri}, dropping below 10 ppm at ϕ_{pri} = 0.95, but exhibits an ascending trend for ϕ_{pri} > 1.2. NH_3 maintains relatively low concentrations in fuel-lean and stoichiometric conditions, signifying a high combustion efficiency. However, for the cases of ϕ_{pri} > 1.0, an excess of fuel supply results in an increase in the unburned NH_3. NO_2 mirrors the trend of NO, with concentrations consistently below 80 ppm across the entire equivalence ratio spectrum.

We next present the improvements on the emissions when applying two-stage combustion. NO markedly diminishes under conditions of ϕ_{pri} < 1, with the peak concentration decreasing from 3690 ppm to 560 ppm, approximately one-seventh as the peak value of the single-stage combustion. However, when ϕ_{pri} > 1, NO emissions exhibit slightly higher values than in single-stage combustion, as illustrated in Fig. 6(a). Fig. 6(b) reveals that N_2O concentration is marginally lower when ϕ_{pri} < 0.7 but significantly higher when ϕ_{pri} > 0.9 compared to single-stage combustion. Moreover, it exhibits a continuous increasing trend. As shown in Fig. 6(c), two-stage combustion effectively mitigates

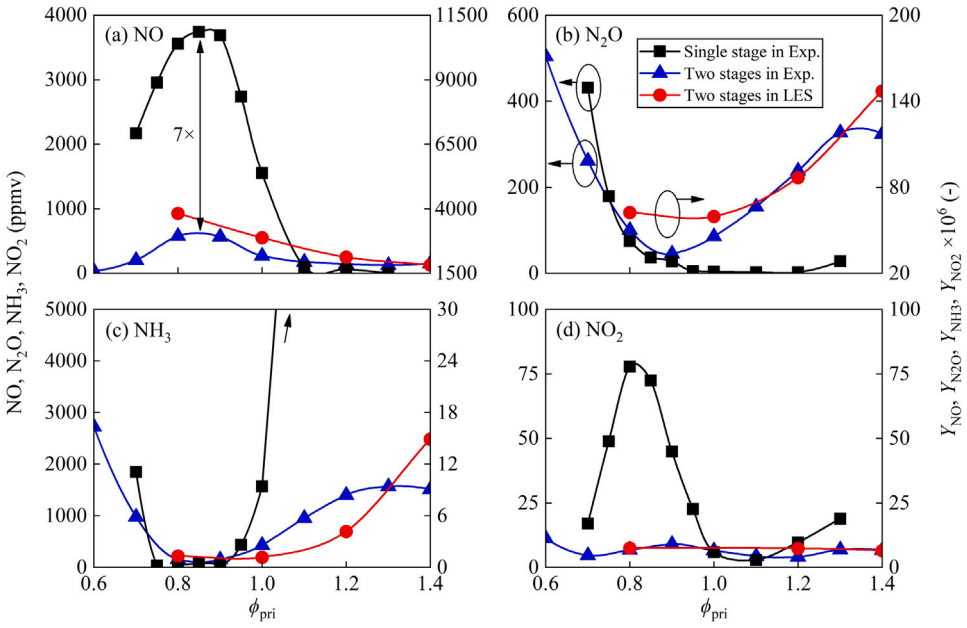

Fig. 6. Emissions corresponding to various primary equivalence ratios, with the overall equivalence ratio maintained at 0.4. (For interpretation of the references to color in this figure legend, the reader is referred to the web version of this article.)

the issue of high NH_3 concentration under primary-rich conditions, resulting in an order of magnitude decreasing in NH_3 slip. Furthermore, as highlighted in Fig. 6(d), the implementation of two-stage combustion approach demonstrates the capacity to decrease NO_2 concentrations to below 20 ppm.

In summary, the adoption of the two-stage combustion strategy yields a substantial reduction in both NO and NO_2 emissions under primary-lean conditions and the decreasing in NH_3 emission under primary-rich conditions. Despite the observed increase in N_2O emission for the cases of $\phi_{pri} > 0.9$, the overall control effect on NOx and ammonia in ammonia–hydrogen co-firing flames is noteworthy. By regulating ϕ_{pri}, it becomes feasible to maintain low concentrations of both NOx and unburned NH_3. With the model combustor in the current study, NOx emissions can be controlled below 200 ppm with the unburned NH_3 goes below 700 ppm without any additional NO reduction process at around $\phi_{pri} = 1.05$. Consequently, this strategy proves to be an effective approach for achieving controlled NOx emissions in ammonia combustion, providing substantial support for the utilization of ammonia as a fuel in gas turbines.

Upon comparing the experimental and simulation results for two-stage combustion in Fig. 6, it is evident that the patterns of emissions concentration variations with ϕ_{pri} obtained from LES are fairly consistent with those from experiments. This implies that the LES-FGM method effectively predicts the production and emission of major pollutants in ammonia–hydrogen co-firing flames. Consequently, this method is employed in subsequent analyses to elucidate the physical and chemical processes occurring inside the combustor after secondary air injection, offering a sound explanation for the observed changes in emissions concentrations.

3.3. Impact of primary equivalence ratios on emissions

Fig. 7 illustrates the instantaneous distribution of NO, OH, NH_3, and H_2 mass fractions in the central cross-section of the chamber under various ϕ_{pri}. The observations reveal that when $\phi_{pri} \leq 1$, the concentration of NO and OH is notably high in the primary zone but significantly decreases upon entering the downstream secondary zone. Conversely, under conditions where $\phi_{pri} > 1$, there is almost no distribution of NO and OH in the primary zone, with their concentrations increasing upon entering the secondary zone, as depicted in Fig. 7(a) and (b). In Fig. 7(c) and (d), it is evident that under primary-lean conditions, NH_3 and H_2 are entirely consumed in the primary zone. However, under primary-rich conditions, residual NH_3 remains in the primary zone. Notably, the H_2 concentration in the primary zone surpasses that in the unburned mixture, indicating the incomplete combustion of ammonia–hydrogen.

Furthermore, a comparison between Figs. 7 (a) and (b) reveals that areas with higher OH concentration tend to produce more NO, while regions with lower OH concentration correspond to relatively lower NO concentration. This observation highlights a noticeable correlation between NO and OH concentrations within the combustion zone. This phenomenon can be attributed to the fact that in ammonia flames NO is primarily generated through the oxidation of NH_i by radicals such as O, H, and OH, leading to the formation of key intermediate species like HNO [5,16,17,37]. The main production paths in Nakamura's mechanism are as follows.

$$NH_2 + O \Leftrightarrow HNO + H \quad \text{(R55)}$$

$$NH + OH \Leftrightarrow HNO + H \quad \text{(R38)}$$

$$HNO + M \Leftrightarrow NO + H + M \quad \text{(R87)}$$

$$HNO + OH \Leftrightarrow NO + H_2O \quad \text{(R90)}$$

$$NH + O \Leftrightarrow NO + H \quad \text{(R42)}$$

For the cases of $\phi_{pri} \leq 1$, a significant quantity of OH is found in the primary zone, promoting the oxidation of NH_2/NH and leading to increased NO production. Concurrently, the fuel in the primary zone is almost consumed. Upon the introduction of secondary air, the significant reduction in OH and NO concentrations in the secondary combustion zone can be primarily attributed to physical dilution [5]. This results in a noticeable reduction in NO concentration at the combustion chamber outlet compared to conditions observed under single-stage combustion. Conversely, for the cases of $\phi_{pri} > 1$, within an environment featuring lower O_2 concentrations and higher NH_i concentrations, the DeNOx effect triggers a substantial reduction of NO [38–40]. With increased involvement of NH_i in reactions with NO, primarily forming N_2 as the major product, the result is a markedly low NO concentration in the primary combustion zone.

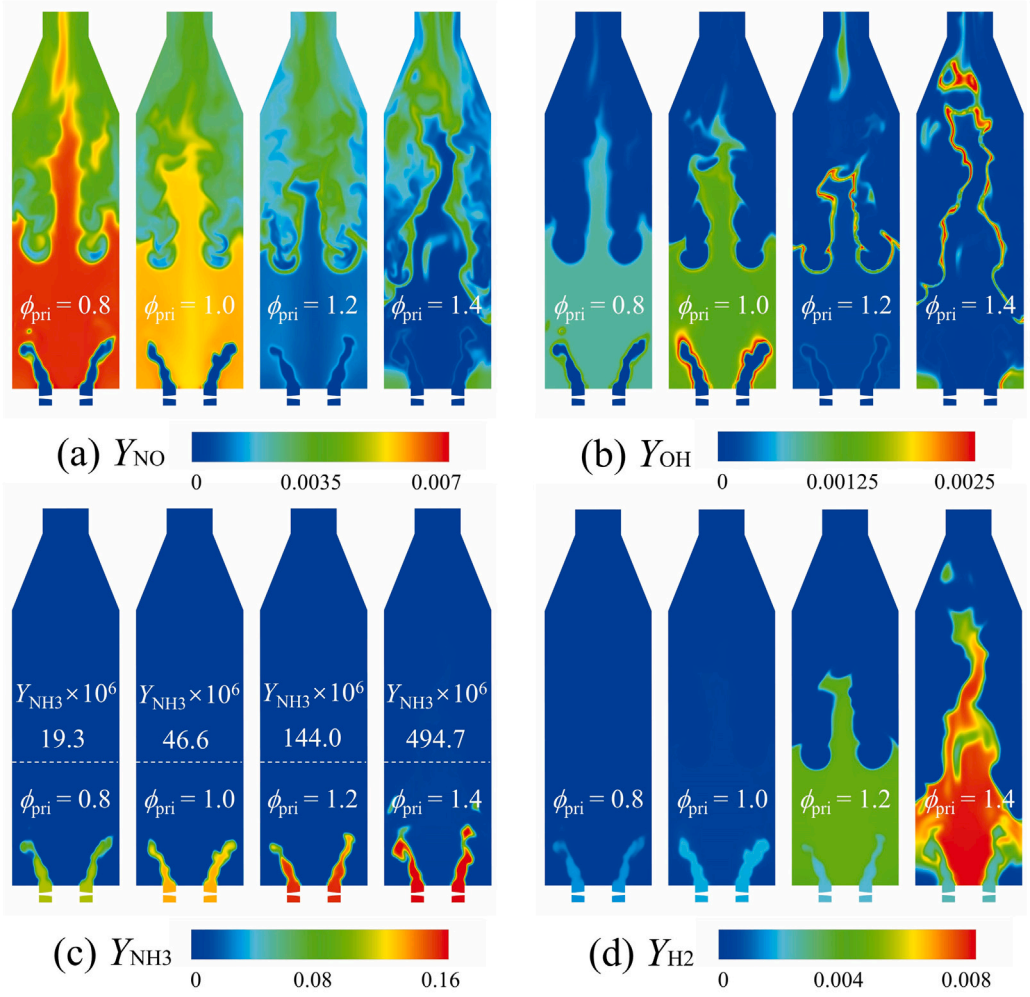

Fig. 7. Instantaneous distributions of NO, OH, NH_3 and H_2 mass fraction in the central cross-section of the combustor at various ϕ_{pri}.

However, under primary-rich conditions, there is a substantial production of H_2 in the primary zone through the reactions $NH_i+H\Leftrightarrow NH_{i-1}+H_2$ [5]. These newly generated H_2 molecules, along with the unburned NH_3, subsequently enter the secondary zone. After the injection of secondary air, H_2 in the secondary combustion zone is initially consumed through reactions $H_2+OH\Leftrightarrow H_2O+H$, $H+O_2\Leftrightarrow OH+O$, and $O+H_2O\Leftrightarrow 2OH$, which results in an increase in H/O/OH radicals. These radicals participate in the oxidation of the remaining NH_3, leading to a substantial production of NO in the secondary combustion zone. This phenomenon elucidates the marginally elevated NO emissions for the cases of $\phi_{pri} > 1$ when using two-stage combustion compared to the single-stage combustion at the same equivalence ratio. Additionally, the lower NH_3 concentration under these conditions also results from this effect.

In order to further reveal the mechanism of NO production in two-stage rich-lean combustion, the relationships between temperature, OH concentration, and NO concentration are analyzed next. Fig. 8 presents pairwise scatter plots of NO mass fraction, OH mass fraction and temperature at the central cross-section of the chamber. The data is categorized based on a horizontal cross-section 80 mm above the bottom of the chamber which helps to separate the primary combustion zone (< 80 mm) and secondary combustion zone (> 80 mm). The location of this cross-section is marked by the white dashed line in Fig. 7(c). Additionally, laminar simulation results are included for the primary zone to facilitate the comparison between the effects of swirl and laminar calculations.

Fig. 8(a) illustrates a strong correlation between the distribution of NO concentration and OH concentration in both primary and secondary combustion zones. Fig. 8(b) and (c) demonstrate that the primary combustion zone with $\phi_{pri} = 1.0$ exhibits the highest temperature along with the maximum OH concentrations. However, it is important to note that, unlike thermal NO, the peak NO concentration does not correspond to the peak temperature. This observation implies that temperature does not play a predominant role in NO production in ammonia flames as analyzed in [41]. Indeed, temperature primarily influences the OH concentration, which subsequently affects NO production. This can be verified by the relatively low OH/NO concentrations in the primary zone for $\phi_{pri} = 1.2$. In contrast, the secondary zone displays a significant increase in OH concentration, coinciding with enhanced NO production. Furthermore, as observed in the first row of Fig. 8, LES results closely align with the laminar results in the primary zone and show a large scatter from the laminar results in the secondary zone. The rationale behind this phenomenon lies in the nature of the turbulent flames examined in this study, which predominantly reside within the thin reaction zone of the turbulent flame regime. In this region, the turbulent disturbance scale is small enough to penetrate into the interior of the flame, only perturbing the preheat zone where chemical reactions are inactive, but not entering the reaction zone. Therefore, small eddies do not affect the combustion chemical reaction process. Additionally, due to the low transport effects in the primary zone, it exhibits characteristics similar to laminar flames. In comparison, NO distribution is determined by a combined effect of chemical production of NO and the species transportation by flow in the secondary zone.

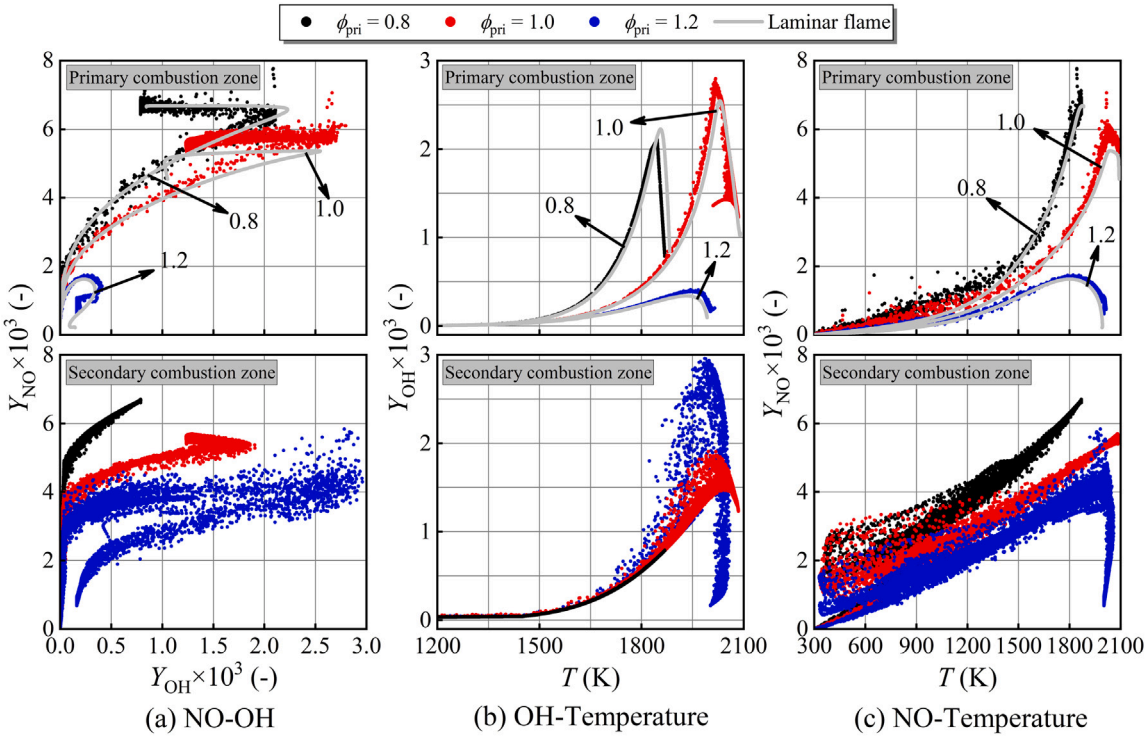

Fig. 8. Relationship between (a) NO and OH; (b) OH and temperature; (c) NO and temperature at the central cross-section of the combustor. The overall equivalence ratio is maintained at 0.4 for all cases.

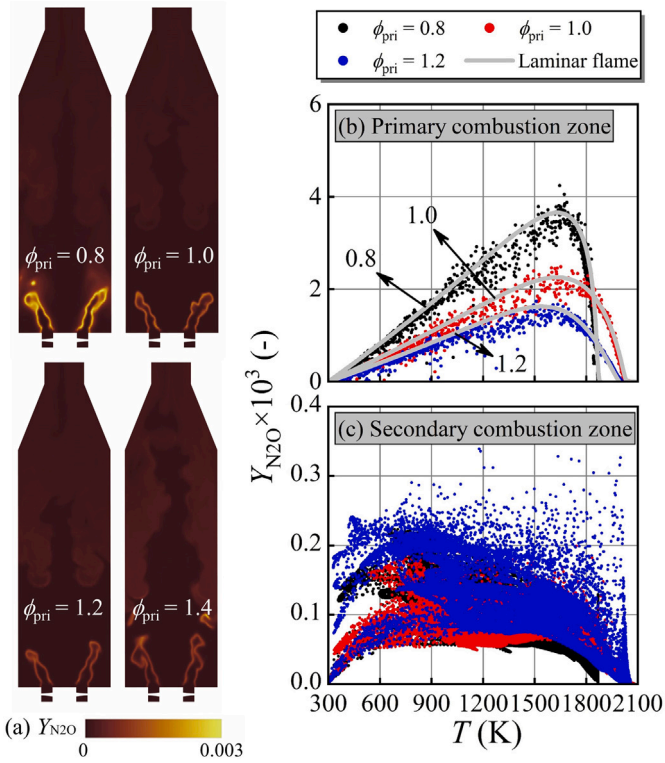

Fig. 9. Instantaneous distributions of N_2O mass fraction in (a) the central cross-section of the combustor at various ϕ_{pri}; Relationship between N_2O and temperature in (b) the primary combustion zone and (c) the secondary combustion zone. The overall equivalence ratio is maintained at 0.4 for all cases.

In ammonia flames, the production of N_2O is primarily driven by the reaction NH+NO⇔N_2O+H [17,34]. Therefore, the concentrations of both NO and NH play a significant role in influencing the production of N_2O. Fig. 9(a) illustrates the distribution of N_2O mass fractions under various ϕ_{pri}. As ϕ_{pri} increases, the concentration of N_2O in the primary zone gradually decreases, as depicted more prominently in Fig. 9(b). The comparison of Fig. 9(a) with Fig. 7(a) reveals that the distribution pattern of N_2O near the primary reaction zone follows the same trend as that of NO, confirming that NO promotes the production of N_2O. Upon entering the secondary combustion zone, it is observed that for both primary-lean and primary-rich conditions, N_2O concentration in the secondary zone is higher than that of the condition of ϕ_{pri} = 1, as shown in Fig. 9(a) and (c).

This can be analyzed from both the perspectives of N_2O production and consumption in the secondary combustion zone. In terms of production, for the cases of $\phi_{pri} \leq 1$, although a significant amount of NO enters the secondary zone, the limited presence of NH_i radicals restricts N_2O production. Concurrently, the dilution effect of the secondary air results in a reduced N_2O emissions for two-stage combustion when compared to single-stage combustion. However, under primary-rich conditions, the injection of secondary air leads to the production of a substantial amount of NO in the secondary zone, as mentioned earlier. Furthermore, the relatively high concentration of NH_i in the secondary zone results in the production of a certain amount of N_2O. This is the primary reason why, the measured N_2O concentration at the combustion chamber outlet is higher than that in single-stage combustion at the same ϕ_{pri}. Regarding N_2O consumption, the primary mechanism for N_2O consumption is thermal decomposition, where the reaction $N_2O(+M)⇔N_2+O(+M)$ is inhibited at lower temperatures [34]. Therefore, the lower temperatures in both primary-lean and primary-rich conditions suppress N_2O consumption, while the higher temperatures in stoichiometric combustion condition result in minimal residual N_2O. The combined effects outlined above contribute to the observed variation in N_2O emissions with changes in ϕ_{pri}, as illustrated in Fig. 6(b).

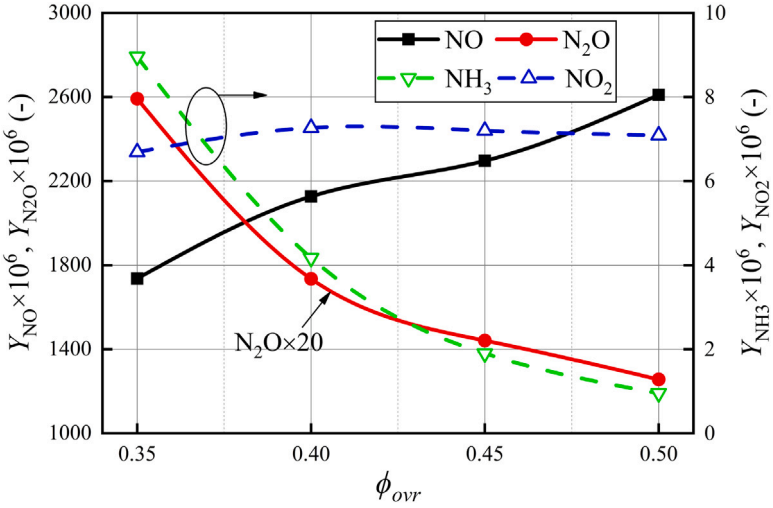

Fig. 10. Variation of space–time-average emissions concentrations obtained from LES with ϕ_{ovr}. The primary equivalence ratio is maintained at 1.2.

3.4. Impact of overall equivalence ratio on emissions

To analyze the impact of ϕ_{ovr} on NOx production and emission, four different values of ϕ_{ovr} are calculated while maintaining a fixed primary equivalence ratio ϕ_{pri} = 1.2. Firstly, the space–time-average NOx as well as NH_3 concentrations are extracted, as shown in Fig. 10. It can be observed that as ϕ_{ovr} increases, the NO emissions gradually increases. However, emissions of unburned NH_3 and N_2O decrease, and the NO_2 concentration remains nearly constant. To clarify the variation in emissions concentrations, iso-surface of heat release rate ($\Omega = 5 \times 10^6$ J/(m^3 s)), symbolizing the flame surface, are extracted and color-coded based on local equivalence ratio (local ϕ), local temperature, OH concentration, and NO concentration, as shown in Fig. 11. It reveals that an increase in ϕ_{ovr} results in a higher flame surface height, signifying an increase in exothermic reactions. This is because, under conditions of a consistent ϕ_{pri}, an increase in ϕ_{ovr} implies a reduced injection of secondary air. As a result, the local ϕ in the secondary zone is relatively higher while still maintaining an overall lean condition, as illustrated in Fig. 11(a). The more suitable oxidizing atmosphere fosters reactions such as $H+O_2 \Leftrightarrow O+OH$, $O+H_2 \Leftrightarrow H+OH$, $OH+H_2 \Leftrightarrow H+H_2O$, and $2OH \Leftrightarrow O+H_2O$, consequently generating a significant quantity of OH/O/H radicals [42]. Within the secondary combustion zone, regions of high temperature and elevated OH concentration on the flame surface intensify, thereby facilitating the effective oxidation of escaping ammonia from the primary combustion zone and reducing NH_3 escape. However, concomitantly, this circumstance unavoidably leads to an increase in NO production, as shown in Fig. 11(b) to (d). Concerning N_2O, the higher NO concentration in the secondary zone resulting from an increase in ϕ_{ovr} undoubtedly promotes its production. However, it is essential to note that the elevated flame temperature in the secondary zone also speeds up the rapid forward reaction of N_2O, represented by the reaction $N_2O(+M) \Leftrightarrow N_2+O(+M)$. This leads to a substantial consumption of N_2O. Based on the final results, it can be inferred that after a reduction in air supply, the amount of N_2O thermally decomposed surpasses the amount newly generated.

The change in ϕ_{ovr}, besides inducing various chemical effects mentioned earlier, should not overlook the alterations in the physical flow field and vortex structures. These changes could also have an impact on the ultimate emissions. In this study, the second invariant Q of the velocity gradient tensor is utilized to characterize vortex structures, with its expression given by Eq. (8).

$$Q = -\frac{1}{2}\frac{\partial \tilde{u}_i}{x_j}\frac{\partial \tilde{u}_j}{x_i} \tag{8}$$

Where u_i (i = 1, 2, 3) represent the velocity components in the Cartesian coordinate system. Variables with over-tildes denote spatial filtering with density weighting, such as $\tilde{f} = \overline{\rho f}/\overline{\rho}$, where, the variables with over-bars represent spatial filtering values obtained from the instantaneous variables [17].

Fig. 12 presents iso-surface of $Q = 1\times10^6$ under different values of ϕ_{ovr}, with coloring based on NO mass fraction. It clearly shows distinct vortex structures in the secondary combustion zone following the introduction of secondary air. This phenomenon is primarily attributed to the tangential swirling effect induced by the injection of secondary air. As the amount of secondary air decreases, this swirling effect weakens, directly leading to a reduction in the scale of vortices, which may influence the local NO concentration. Study by De et al. [43] suggested that NO production is sensitive to residence time. With an increase in ϕ_{ovr}, the reduction in vortex scale leads to a decrease in residence time, resulting in a trend of reduced NO concentration in the vortex, as depicted in Fig. 12. These observations align with the findings of An et al. [26]. However, it is important to note that the impact of changes in vortex structures on NO production is incomparable to the dominating chemical effects discussed earlier. This is because an increase in ϕ_{ovr} ultimately leads to an upward trend in NO concentration, indicating that chemical reactions play a predominant role in this process.

4. Conclusions

The effects of the primary equivalence ratio ϕ_{pri} and overall equivalence ratio ϕ_{ovr} on NOx and NH_3 emissions were studied with a two-stage combustion strategy for ammonia–hydrogen co-firing flames. Emissions of the experimental flames were measured using FTIR. The chemical and physical effects governing emission generation were investigated with the LES-FGM method. The main conclusions obtained are as follows:

1. The two-stage combustion strategy exhibits noteworthy effects in emissions control of the ammonia swirling flames. When $\phi_{pri} < 1$, NO and NO_2 concentrations can be decreased to roughly one-seventh of the single-stage combustion conditions. With the current model combustor, NOx emissions can be controlled below 200 ppm with the unburned NH_3 not greater than 700 ppm at around $\phi_{pri} = 1.05$ and $\phi_{ovr} = 0.4$.
2. ϕ_{pri} plays a pivotal role in determining the temperature and OH concentration in the primary combustion zone, thus impacting the production of NOx in this zone. Under conditions of $\phi_{pri} \leq 1$, the primary zone exhibits a high OH concentration, leading to

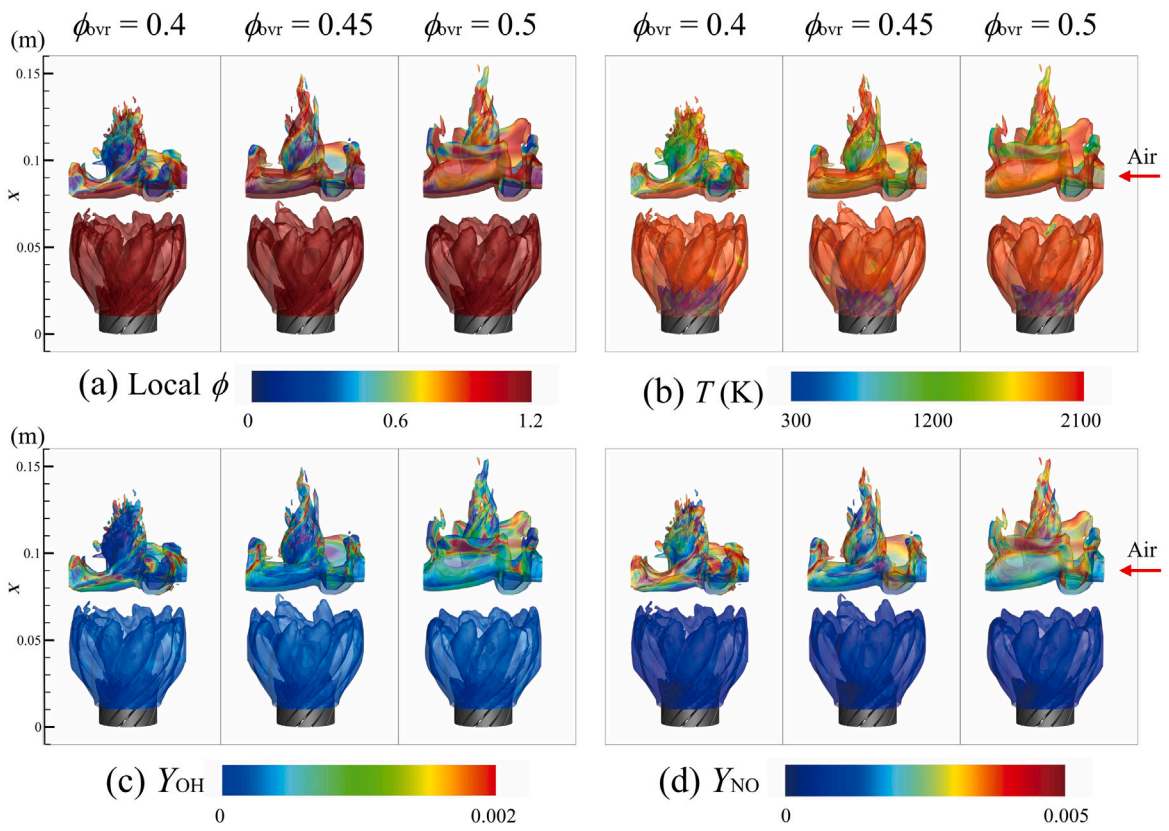

Fig. 11. The flame structure at various ϕ_{ovr}. The flame surface is indicated by heat release rate iso-surface $\Omega = 5 \times 10^6$ J/(m^3 s), colored by local ϕ, temperature, OH mass fraction, and NO mass fraction, respectively.

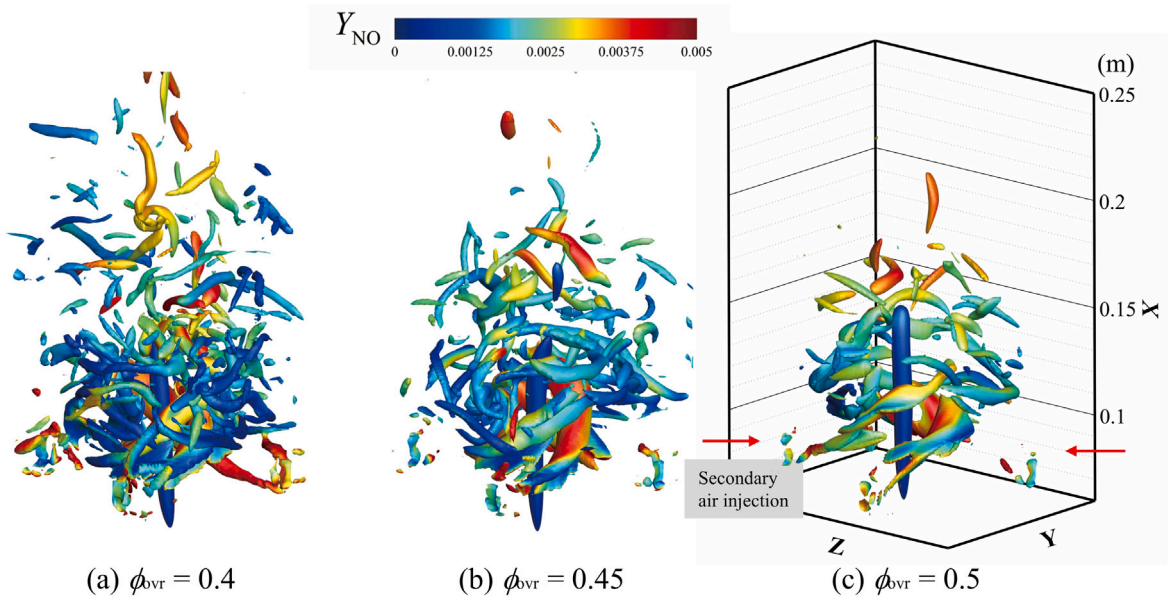

Fig. 12. The vortex structures in the secondary combustion zone at various ϕ_{ovr}. The vortices are represented by iso-surface of the second invariant of the velocity gradient tensor $Q = 1{\times}10^6$, colored by NO mass fraction.

the substantial production of NO through the key intermediate species HNO. NO emission was largely affected by the dilution effect of secondary air. When $\phi_{pri} > 1$, the lower OH concentration in the primary zone inhibits the NO production. However, further increasing ϕ_{pri} will lead to larger unburned NH_3 and H_2 which will produce some NO in the secondary zone, resulting the optimal ϕ_{pri} being around 1.2.

3. ϕ_{ovr} shows two considerable effects. On the one hand, with an increase in ϕ_{ovr}, the secondary zone demonstrates a higher local equivalence ratio, thereby promoting local NOx production. Additionally, the elevated flame temperature enhances the consumption of N_2O. On the other hand, the rise in ϕ_{ovr} results in a reduction in vortex scale and residence time in the secondary combustion zone, leading to a decrease in local NO production.

However, this effect is relatively weak compared to the impact of chemical reactions.

CRediT authorship contribution statement

Liqing Lu: Data curation, Investigation, Writing – original draft, Formal analysis. **Meng Zhang:** Conceptualization, Funding acquisition, Supervision, Writing – review & editing, Project administration. **Weijie Zhang:** Methodology. **Lei Chen:** Methodology, Resources. **Pengfei Song:** Methodology, Resources. **Zhilong Wei:** Resources, Writing – review & editing. **Jinhua Wang:** Funding acquisition, Writing – review & editing. **Zuohua Huang:** Funding acquisition, Project administration.

Declaration of competing interest

The authors declare that they have no known competing financial interests or personal relationships that could have appeared to influence the work reported in this paper.

Acknowledgments

This study is financially supported by the National Natural Science Foundation of China (No. 52176130). Authors also express their greatly appreciation on the great effort of Dr. Xutao Wei, Mr. Ruixiang Wang and Jian Chen during the experiments.

References

[1] Kobayashi H, Hayakawa A, Somarathne KKA, Okafor EC. Science and technology of ammonia combustion. Proc Combust Inst 2019;37(1):109–33.
[2] Li S, Zhang S, Zhou H, Ren Z. Analysis of air-staged combustion of NH3/CH4 mixture with low NOx emission at gas turbine conditions in model combustors. Fuel 2019;237:50–9.
[3] Zhu X, Khateeb AA, Guiberti TF, Roberts WL. NO and OH* emission characteristics of very-lean to stoichiometric ammonia–hydrogen–air swirl flames. Proc Combust Inst 2021;38(4):5155–62.
[4] Hayakawa A, Goto T, Mimoto R, Arakawa Y, Kudo T, Kobayashi H. Laminar burning velocity and Markstein length of ammonia/air premixed flames at various pressures. Fuel 2015;159:98–106.
[5] Okafor EC, Somarathne KKA, Ratthanan R, Hayakawa A, Kudo T, et al. Control of NOx and other emissions in micro gas turbine combustors fuelled with mixtures of methane and ammonia. Combust Flame 2020;211:406–16.
[6] Valera-Medina A, Xiao H, Owen-Jones M, David W, Bowen P. Ammonia for power. Prog Energy Combust Sci 2018;69:63–102.
[7] Lee J, Kim J, Park J, Kwon O. Studies on properties of laminar premixed hydrogen-added ammonia/air flames for hydrogen production. Int J Hydrogen Energy 2010;35(3):1054–64.
[8] Zhang M, An Z, Wang L, Wei X, Jianayihan B, Wang J, et al. The regulation effect of methane and hydrogen on the emission characteristics of ammonia/air combustion in a model combustor. Int J Hydrogen Energy 2021;46(40):21013–25.
[9] Vignat G, Zirwes T, Toro ER, Younes K, Boigné E, Muhunthan P, et al. Experimental and numerical investigation of flame stabilization and pollutant formation in matrix stabilized ammonia-hydrogen combustion. Combust Flame 2023;250:112642.
[10] Franco MC, Rocha RC, Costa M, Yehia M. Characteristics of NH3/H2/air flames in a combustor fired by a swirl and bluff-body stabilized burner. Proc Combust Inst 2021;38(4):5129–38.
[11] Khateeb AA, Guiberti TF, Wang G, Boyette WR, Younes M, Jamal A, et al. Stability limits and NO emissions of premixed swirl ammonia-air flames enriched with hydrogen or methane at elevated pressures. Int J Hydrogen Energy 2021;46(21):11969–81.
[12] Valera-Medina A, Morris S, Runyon J, Pugh D, Marsh R, Beasley P, et al. Ammonia, methane and hydrogen for gas turbines. Energy Procedia 2015;75:118–23.
[13] Valera-Medina A, Pugh D, Marsh P, Bulat G, Bowen P. Preliminary study on lean premixed combustion of ammonia-hydrogen for swirling gas turbine combustors. Int J Hydrogen Energy 2017;42(38):24495–503.
[14] Valera-Medina A, Gutesa M, Xiao H, Pugh D, Giles A, Goktepe B, et al. Premixed ammonia/hydrogen swirl combustion under rich fuel conditions for gas turbines operation. Int J Hydrogen Energy 2019;44(16):8615–26.
[15] Mashruk S, Kovaleva M, Alnasif A, Chong CT, Hayakawa A, Okafor EC, et al. Nitrogen oxide emissions analyses in ammonia/hydrogen/air premixed swirling flames. Energy 2022;260:125183.
[16] Somarathne KDKA, Hatakeyama S, Hayakawa A, Kobayashi H. Numerical study of a low emission gas turbine like combustor for turbulent ammonia/air premixed swirl flames with a secondary air injection at high pressure. Int J Hydrogen Energy 2017;42(44):27388–99.
[17] Somarathne KDKA, Okafor EC, Hayakawa A, Kudo T, Kurata O, Iki N, et al. Emission characteristics of turbulent non-premixed ammonia/air and methane/air swirl flames through a rich-lean combustor under various wall thermal boundary conditions at high pressure. Combust Flame 2019;210:247–61.
[18] Tian Z, Li Y, Zhang L, Glarborg P, Qi F. An experimental and kinetic modeling study of premixed NH3/CH4/O2/Ar flames at low pressure. Combust Flame 2009;156(7):1413–26.
[19] Li Z, Li S. Kinetics modeling of NOx emissions characteristics of a NH3/H2 fueled gas turbine combustor. Int J Hydrogen Energy 2021;46(5):4526–37.
[20] Li Z, Zhang Y, Zhang H. Kinetics modeling of NOx emission of oxygen-enriched and rich-lean-staged ammonia combustion under gas turbine conditions. Fuel 2024;355:129509.
[21] Mashruk S, Xiao H, Valera-Medina A. Rich-Quench-Lean model comparison for the clean use of humidified ammonia/hydrogen combustion systems. Int J Hydrogen Energy 2021;46(5):4472–84.
[22] Guteša Božo M, Vigueras-Zuniga M, Buffi M, Seljak T, Valera-Medina A. Fuel rich ammonia-hydrogen injection for humidified gas turbines. Appl Energy 2019;251:113334.
[23] Guteša Božo M, Mashruk S, Zitouni S, Valera-Medina A. Humidified ammonia/hydrogen RQL combustion in a trigeneration gas turbine cycle. Energy Convers Manage 2021;227:113625.
[24] Wei X, Zhang M, Wang J, Huang Z. Investigation on lean blow-off characteristics and stabilization mechanism of premixed hydrogen enhanced ammonia/air swirl flames in a gas turbine combustor. Combust Flame 2023;249:112600.
[25] Zhang M, Xu W, Wang R, Wei X, Wang J, Huang Z, et al. Wall heat loss effect on the emission characteristics of ammonia swirling flames in a model gas turbine combustor. Combust Flame 2023;256:112955.
[26] An Z, Zhang M, Zhang W, Mao R, Wei X, Wang J, et al. Emission prediction and analysis on CH4/NH3/air swirl flames with LES-FGM method. Fuel 2021;304:121370.
[27] van Oijen J. Flamelet-generated manifolds: development and application to premixed laminar flames. Eindhoven University Press; 2002.
[28] van Oijen J, Donini A, Bastiaans R, ten Thije Boonkkamp J, de Goey L. State-of-the-art in premixed combustion modeling using flamelet generated manifolds. Prog Energy Combust Sci 2016;57:30–74.
[29] Zhang W, Karaca S, Wang J, Huang Z, van Oijen J. Large eddy simulation of the cambridge/sandia stratified flame with flamelet-generated manifolds: Effects of non-unity lewis numbers and stretch. Combust Flame 2021;227:106–19.
[30] Chem1D. A one-dimensional laminar flame code. Eindhoven University of Technology; 2016.
[31] Nakamura H, Hasegawa S, Tezuka T. Kinetic modeling of ammonia/air weak flames in a micro flow reactor with a controlled temperature profile. Combust Flame 2017;185:16–27.
[32] Bioche K, Bricteux L, Bertolino A, Parente A, Blondeau J. Large eddy simulation of rich ammonia/hydrogen/air combustion in a gas turbine burner. Int J Hydrogen Energy 2021;46(79):39548–62.
[33] Chen J, Jiang X, Qin X, Huang Z. Effect of hydrogen blending on the high temperature auto-ignition of ammonia at elevated pressure. Fuel 2021;287:119563.
[34] Hayakawa A, Hayashi M, Kovaleva M, Gotama GJ, Okafor EC, Colson S, et al. Experimental and numerical study of product gas and N2O emission characteristics of ammonia/hydrogen/air premixed laminar flames stabilized in a stagnation flow. Proc Combust Inst 2023;39(2):1625–33.
[35] Honzawa T, Kai R, Okada A, Valera-Medina A, Bowen PJ, Kurose R. Predictions of NO and CO emissions in ammonia/methane/air combustion by LES using a non-adiabatic flamelet generated manifold. Energy 2019;186:115771.
[36] Hayakawa A, Goto T, Mimoto R, Kudo T, Kobayashi H. NO formation/reduction mechanisms of ammonia/air premixed flames at various equivalence ratios and pressures. Mech Eng J 2015;2. 14–00402–14–00402.
[37] Okafor EC, Somarathne KKA, Hayakawa A, Kudo T, Kurata O, Iki N, et al. Towards the development of an efficient low-NOx ammonia combustor for a micro gas turbine. Proc Combust Inst 2019;37(4):4597–606.
[38] Klippenstein SJ, Harding LB, Glarborg P, Miller JA. The role of NNH in NO formation and control. Combust Flame 2011;158(4):774–89.
[39] Glarborg P, Miller JA, Ruscic B, Klippenstein SJ. Modeling nitrogen chemistry in combustion. Prog Energy Combust Sci 2018;67:31–68.

[40] Pacheco GP, Rocha RC, Franco MC, Mendes MAA, Fernandes EC, Coelho PJ, et al. Experimental and kinetic investigation of stoichiometric to rich NH3/H2/Air flames in a swirl and bluff-body stabilized burner. Energy Fuels 2021;35:7201–16.

[41] Somarathne KDKA, Okafor EC, Sugawara D, Hayakawa A, Kobayashi H. Effects of OH concentration and temperature on NO emission characteristics of turbulent non-premixed CH4/NH3/air flames in a two-stage gas turbine like combustor at high pressure. Proc Combust Inst 2021;38(4):5163–70.

[42] Chaturvedi S, Santhosh R, Mashruk S, Yadav R, Valera-Medina A. Prediction of NOx emissions and pathways in premixed ammonia-hydrogen-air combustion using CFD-CRN methodology. J Energy Inst 2023;111:101406.

[43] Toni AD, Hayashi T, Schneider P. A reactor network model for predicting NOx emissions in an industrial natural gas burner. J Braz Soc Mech Sci Eng 2013;35:199–206.